1	Blocked radiative heat transport in the hot pyrolitic lower mantle
2	Sergey S. Lobanov <sup>1,2,3,*</sup> , Nicholas Holtgrewe <sup>1,4</sup> , Gen Ito <sup>2</sup> , James Badro <sup>5</sup> , Helene Piet <sup>6</sup>
3	Farhang Nabiei <sup>6,7</sup> , Jung-Fu Lin <sup>8</sup> , Lkhamsuren Bayarjargal <sup>9</sup> , Richard Wirth <sup>3</sup> , Anja
4	Schreiber <sup>3</sup> , Alexander F. Goncharov <sup>1,10</sup>
5	<sup>1</sup> Geophysical Laboratory, Carnegie Institution of Washington, Washington, DC 20015,
6	USA
7	<sup>2</sup> Department of Geosciences, Stony Brook University, Stony Brook, NY 11794, USA
8	<sup>3</sup> Helmholtz Center Potsdam, GFZ German Research Center for Geosciences,
9	Telegrafenberg, 14473 Potsdam, Germany
10	<sup>4</sup> Center for Advanced Radiation Sources, University of Chicago, IL 60637, USA
11	<sup>5</sup> Institut de Physique du Globe de Paris, Sorbonne Paris Cite, Paris 75005, France
12	<sup>6</sup> Earth and Planetary Science Laboratory, Ecole Polytechnique Fédérale de Lausanne,
13	CH-1015 Lausanne, Switzerland
14	<sup>7</sup> Centre Interdisciplinaire de Microscopie Electronique, Ecole Polytechnique Fédérale de
15	Lausanne, CH-1015 Lausanne, Switzerland
16	<sup>8</sup> Department of Geological Sciences, Jackson School of Geosciences, The University of
17	Texas at Austin, Austin, TX 78712, USA
18	<sup>9</sup> Institute of Geosciences, Goethe University Frankfurt am Main, Frankfurt am Main,
19	Germany
20	<sup>10</sup> Key Laboratory of Materials Physics, Institute of Solid State Physics CAS, Hefei
21	230031, China
22	*E-mail: slobanov@gfz-potsdam.de

#### Abstract

The heat flux across the core-mantle boundary ( $Q_{CMB}$ ) is the key parameter to understand the Earth's thermal history and evolution. Mineralogical constraints of the  $Q_{CMB}$  require deciphering contributions of the lattice and radiative components to the thermal conductivity at high pressure and temperature in lower mantle phases with depth-dependent composition. Here we determine the radiative conductivity ( $k_{rad}$ ) of a realistic lower mantle (pyrolite) in situ using an ultra-bright light probe and fast time-resolved spectroscopic techniques in laser-heated diamond anvil cells. We find that the mantle opacity increases critically upon heating to ~3000 K at 40-135 GPa, resulting in an unexpectedly low radiative conductivity decreasing with depth from ~0.8 W/m/K at 1000 km to ~0.35 W/m/K at the CMB, the latter being ~30 times smaller than the estimated lattice thermal conductivity at such conditions. Thus, radiative heat transport is blocked due to an increased optical absorption in the hot lower mantle resulting in a moderate CMB heat flow of ~8.5 TW, on the lower end of previous  $Q_{CMB}$  estimates based on the mantle and core dynamics. This moderate rate of core cooling implies an inner core age of about 1 Gy and is compatible with both thermally- and compositionally-driven ancient geodynamo.

# Keywords

Thermal conductivity; high pressure; time-resolved spectroscopy; core-mantle boundary; diamond anvil cell

## 1. Introduction

Heat exchange rate between the mantle and core ( $Q_{CMB}$ ) is of primary importance for mantle convection and core geodynamo, the two processes that have been paramount for life on Earth. Considerations of the mantle and core energy budgets suggest a  $Q_{CMB}$  in the range of 10-16 TW (e.g. Nimmo (2015)). Independently, transport properties of the mantle can provide

insights into the  $Q_{CMB}$  as it is controlled by the thermal conductivity of the mantle rock at the core-mantle boundary (CMB). Total thermal conductivity of primary lower mantle minerals is a sum of its lattice and radiative components ( $k_{total} = k_{lat} + k_{rad}$ ). At near-ambient temperatures ( $T \sim 300 \text{ K}$ ) the dominant mechanism of heat conduction is lattice vibrations while radiative transport is minor. At high temperature, however, the radiative mechanism is expected to become much more effective (Clark, 1957) as  $k_{rad}(P,T) \sim \frac{T^3}{\alpha(P,T)}$  (Eq.1), where  $\alpha(P,T)$  is the pressure- and temperature-dependent light absorption coefficient of the conducting medium. Mantle  $k_{rad}$  is expected to increase with depth and light radiation might even be the dominant mechanism of heat transport in the hot thermal boundary layer (TBL) a few hundred km above the core (Hofmeister, 2014; Keppler et al., 2008). To reconstruct mantle radiative thermal conductivity one needs to know the absorption coefficient of representative minerals in the near-infrared (IR) and visible (VIS) range collected at P-T along the geotherm.

Light diffusion in the hot lower mantle is governed by absorption mechanisms in iron-bearing bridgmanite (Bgm), post-preovskite (Ppv), and ferropericlase (Fp) as these minerals have absorption bands in the near-infrared (IR) and visible (VIS) range (Goncharov et al., 2009; Goncharov et al., 2008; Goncharov et al., 2015; Keppler et al., 2008). The intensity and position of absorption bands in the spectra of iron-bearing minerals vary with pressure (Goncharov et al., 2009; Goncharov et al., 2008; Goncharov et al., 2015; Keppler et al., 2008) and temperature (Lobanov et al., 2017; Thomas et al., 2012; Ullrich et al., 2002). For example, previous room-temperature studies identified an increase in the absorption coefficient of Fp up to 135 GPa associated primarily with the spin transition and red-shift of the Fe-O charge transfer band (Goncharov et al., 2006; Keppler et al., 2007). Likewise, studies of upper mantle minerals at moderate temperatures have recognized substantial variations in their absorption spectra in the IR-VIS range. Crystal field and Fe-O charge transfer bands in olivine show an apparent intensification and broadening upon heating to 1700 K at 1 atm (Ullrich et al., 2002). Similarly, characteristics of the Fe<sup>2+</sup>-Fe<sup>3+</sup> charge transfer bands in wadsleyite and ringwoodite are altered

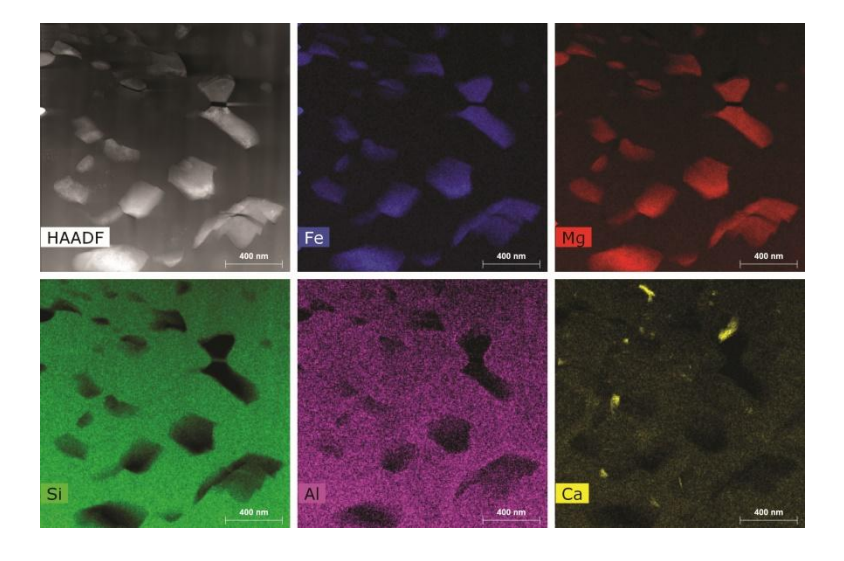
upon heating to ~800 K (Thomas et al., 2012). Although these transformations cannot be reliably extrapolated to temperatures of several thousand Kelvin, similar absorption mechanisms govern the optical properties of Bgm, Fp, and Ppv in the lower mantle, and thus must affect their radiative conductivity. Despite the importance, optical properties of Bgm, Ppv, and Fp have never been measured at mantle P-T conditions as such measurements are challenging because of the thermal radiation interfering with the probe light at high T. On top of the P- and T-dependence of optical properties, absorption coefficients are sensitive to iron concentration, its valence/spin state, and crystallographic environment. In the mantle all of these vary with depth in a complex and not yet fully understood way (Irifune et al., 2010), contributing to the uncertainty in the mantle  $k_{rad}$ . As a result of these complications, current  $k_{rad}$  models are exclusively based on room-temperature measurements of Bgm and Fp with fixed chemical composition (Goncharov et al., 2009; Goncharov et al., 2008; Goncharov et al., 2015; Keppler et al., 2008).

# 2. Experimental Methods

Optical measurements at high *P-T* were performed in laser-heated diamond anvil cells (DACs) using an ultra-bright light probe synchronized with fast time-resolved IR and VIS detectors that allowed us to diminish the contribution of thermal background (more details are provided in Supplementary Materials). We determine the radiative conductivity of the lower mantle by measuring the spectral optical depth in pyrolite, a chemical proxy of the mantle (Irifune et al., 2010), along the Earth's geotherm. Samples of highly homogeneous pyrolite glass (Supplementary Table S1) were crystallized at the thermodynamic conditions of the lower mantle producing a conglomerate of Bgm (±Ppv) and Fp with compositions representative of the equilibrium in the lower mantle (Fig. 1). The latter allowed us to account for the effects of *P*-and *T*-dependent crystal chemistry such as the iron content and its valence/spin states in the lower mantle phases.

Prior to optical measurements, each glass sample was crystallized at P > 30 GPa and T up

to 3000 K for several minutes. Full glass crystallization was confirmed by the disappearance of a diffuse low frequency Raman peak (boson peak), which is characteristic of glasses (Supplementary Fig. S1). The mineralogical content of all crystalized samples is dominated by Bgm (+ Ppv at  $\sim$ 135 GPa) and Fp as revealed by the synchrotron x-ray diffraction (XRD) (Supplementary Fig. S2). In addition to XRD characterization, one of the recovered pyrolite samples (~2800 K and 56 GPa) was further analyzed using scanning transmission electron microscopy (STEM) and energy-dispersive x-ray spectroscopy (EDX) in order reveal its fine texture and the chemical composition of constituting minerals (see details on analytical techniques in Supplementary Materials). High-angle annular dark-field (HAADF) images show that the average grain size of the crystallized pyrolite is smaller than  $\sim 500$  nm (Fig. 1), suggesting that light scattering on grain boundaries might be substantial (Hulst, 1957) and needs to be taken into account. The bulk of the crystallized sample is composed of Bgm, Fp, and Caperovskite in the proportions that are consistent with the previous reports on pyrolite mineralogy (~75, 18, and 7 vol.%, respectively (Irifune et al., 2010). Coexisting Bgm and Fp are homogeneous in their chemical composition and show no significant variations across the probed areas with Bgm  $^{Fe\#}=7.7\pm\sim2$  and  $Fp^{Fe\#}=16.8\pm\sim2$  (Supplementary Table S2), also in agreement with that reported in the literature (e.g. Irifune et al. (2010)). In addition to Bgm, Fp, and Caperovskite, we have also observed scarce grains of metallic Fe (< ~1 vol.%), supporting the notion that the lower mantle may contain a small amount of metallic iron-rich alloy.



99

100

101

102

103

104

105

106

107

108

109

110

111

112

113

114

115

116

## 3. Results and Discussion

Upon heating, our IR-VIS measurements reveal that the optical absorbance of pyrolite shows a continuous strong increase up to the maximum temperature of ~2855 K at all studied pressures (Supplementary Fig. S4 and S5). Importantly, the observed temperature-enhanced absorption is reversible, as is indicated by the similarity of absorption coefficients measured prior and after the laser-heating cycles, suggesting that the increased opacity at high *T* is due to a temperature-activated absorption mechanism in the IR-VIS range. Figure 2 shows pyrolite absorption coefficient at selected *P-T* conditions that approximate the Earth's geotherm with the exception of the spectrum measured at 134 GPa and 2780 K. The absorption coefficient of pyrolite increases by a factor of 4-8 (depending on the frequency) from 40 GPa / 2120 K to 134 GPa / 2780 K. An even larger absorption coefficient might be expected for the CMB temperatures of ~4000 K. Accordingly, we extrapolated the 134 GPa absorption coefficient to 4000 K using its near-linear temperature dependence established in the 1700-2700 K range (Supplementary Materials Fig. S6).

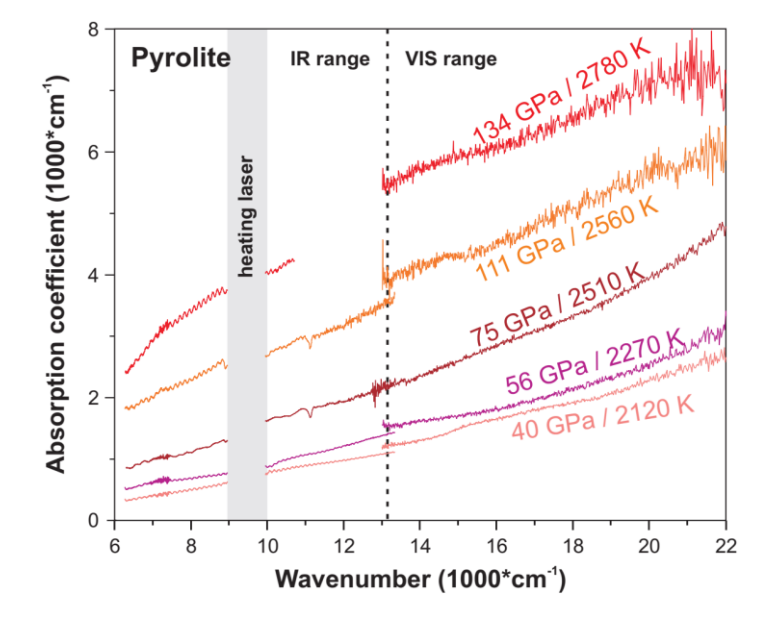


**Figure 2.** Pyrolite absorption coefficient at high *P-T* (before scattering correction). Vertical dashed line separates the IR and VIS ranges as these were measured separately. The 9000-1000 cm<sup>-1</sup> region is blocked because of the need to filter out the 1070 nm heating laser radiation from reaching the detector. The 11000-13000 cm<sup>-1</sup> region in the 134 GPa / 2710 K spectrum (red) is not shown because of the poor signal-to-background ratio of the IR detector in this range at high absorbance levels.

138

139

140

141

142

143

144

145

146

147

148

149

150

151

152

153

154

155

156

157

158

159

160

161

162

163

The radiative conductivity of an absorbing medium is given by (Clark, 1957):  $k_{rad}(T) =$  $\frac{4n^2}{3}\int_0^\infty \frac{1}{\alpha(v)} \frac{\partial I(v,T)}{\partial T} dv$  (Eq.2), where  $\alpha(v)$  is the frequency-dependent absorption coefficient of the medium, n its refractive index, and I(v, T) is the Planck function. Prior to  $k_{rad}$  evaluation, all absorption coefficients were corrected for light scattering in a submicron-grained sample based on the room-temperature absorption coefficients of single crystalline Bgm and Fp with corresponding compositions, which were measured separately using a different optical setup with a conventional (non-laser) optical probe (Goncharov et al., 2009) (Supplementary Materials Fig. S7). Scattering-corrected absorption coefficients measured at P-T conditions approximating the geotherm yield  $k_{rad}$  values that decrease continuously with depth from ~0.8 W/m/K at 1000 km to  $\sim 0.1$  W/m/K at the top of the TBL (at  $\sim 2500$  km) and then increases to  $\sim 0.35$  W/m/K at the CMB (Fig. 3). Even smaller  $k_{rad}$  values may be expected for the lower mantle if its grain size is smaller than the optical depth of pyrolite (< 100 µm) due to light scattering on grain boundaries. However, the grain size of the mantle is likely larger than the photon mean free path because of the hot regime favoring grain growth (e.g. Keppler et al. (2008)). The apparent negative slope of radiative thermal conductivity with depth is at odds with all previous radiative conductivity models, which show a positive trend and  $k_{rad}$  up to 4-5 W/m/K at the CMB (Goncharov et al., 2015; Hofmeister, 2014; Keppler et al., 2008). These previous models, however, were based on room-temperature measurements (Goncharov et al., 2008; Goncharov et al., 2015; Keppler et al., 2008) or empirical considerations on the transparency of silicates at high temperature that assumed negligible temperature effect on the mantle optical properties (Hofmeister, 2014). Here we showed that pyrolite optical properties are highly sensitive to T

(Supplementary Materials Fig. S4 and S5), suggesting that temperature-enhanced absorption coefficient leads to the negative  $k_{rad}$  slope with depth.

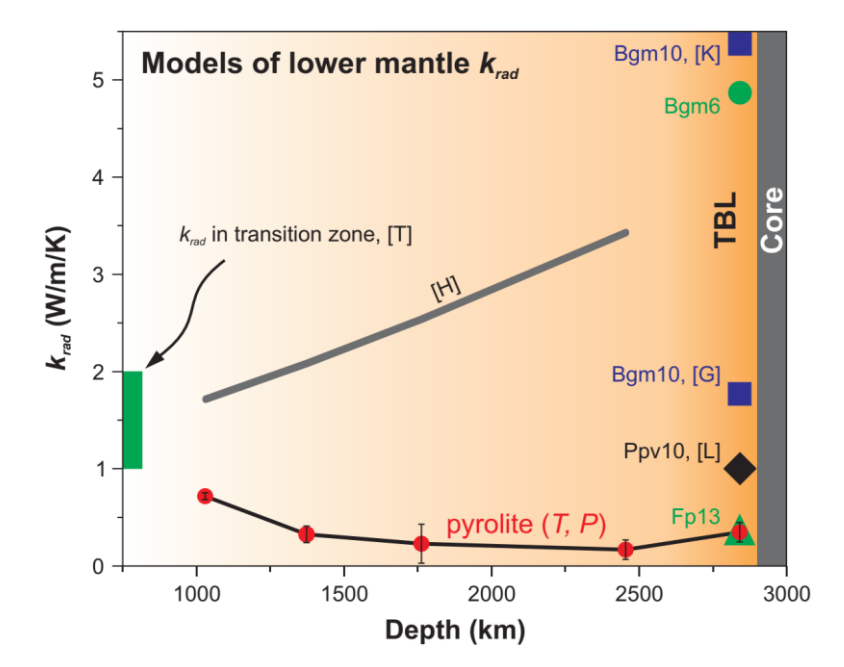


**Figure 3.** Radiative conductivity of the pyrolitic lower mantle along the geotherm (Stacey and Davis, 2008)

(red circles). The error bars vary with depth and reflect the quality of our scattering correction and uncertainty in the sample thickness at high pressure (Supplementary Materials). The absorption coefficient for 2850 km was projected to 4000 K assuming a linear temperature-dependence of absorbance at T > 2780 K (Supplementary Fig. 86). Green circle and triangle are  $k_{rad}$  values of Bgm and Fp with 6 and 13 mol.% Fe, respectively, based on their single crystal absorption coefficients measured at 117 GPa and 300 K (Supplementary Fig. 87). Grey thick curve marked [H] is the thermodynamic model of Hofmeister (2014): $k_{rad} = 1.9 * 10^{-10} * T^3$ . Dark blue squares are  $k_{rad}$  of Bgm with 10 mol.% Fe based on its 300 K absorption coefficient reported by Keppler et al. (2008) and Goncharov et al. (2015), marked [K] and [G]. Black diamond [L] is  $k_{rad}$  of Ppv with 10 mol.% Fe (Lobanov et al., 2017). Green bar [T] is the range of  $k_{rad}$  values expected in the transition zone (Thomas et al., 2012). TBL is for thermal boundary layer above the core-mantle boundary. The color gradation illustrates the distribution of temperature in the lower mantle.

Light absorption in pyrolite at high P-T is governed by specific absorption mechanisms in its constituent phases. In order to disentangle the contribution of Bgm and Fp to the high-temperature spectra of pyrolite we measured the absorption coefficient of Bgm (single crystal, 6 mol.% Fe) up to  $\sim$ 2500 K (Supplementary Fig. S8). Surprisingly, the absorption coefficient of Bgm increases with the rate of  $\sim$ 0.1 cm<sup>-1</sup>/K, while a much stronger temperature-dependence of

 $\sim$ 0.4 cm<sup>-1</sup>/K is characteristic of pyrolite (Supplementary Fig. S6). This observation hints that the strong increase in pyrolite absorbance at high temperature is not due to Bgm but is a result of the temperature-enhanced opacity of Fp. Unfortunately, we could not obtain reliable high-temperature absorption spectra of Fp as it showed irreversible changes in absorbance over continuous laser heating at T > 1000 K. We tentatively attribute this behavior to Soret-like iron diffusion under the steep temperature gradient typical of laser-heated samples. Cation diffusion rates in Fp are  $\sim$ 2 orders of magnitude faster than in Bgm (Ammann et al., 2010), which may be why reversible spectroscopic behavior is preserved in Bgm upon continuous laser heating up to T > 2500 K. In the pyrolite sample iron diffusion is further limited by the small grain size and the reversible spectroscopic behavior is preserved up to  $\sim$ 3000 K (at 134 GPa).

To suppress iron diffusion and directly compare the temperature-induced changes in the Bgm and Fp optical absorbance we decreased the total laser-heating time by a factor of  $\sim 10^6$  in an independent series of dynamically-heated DAC experiments. Fully reversible optical absorbance was observed in Bgm and Fp over the single-shot 1  $\mu$ s long laser-heating to T > 3000K at 111-135 GPa (Supplementary Fig. S9). Upon heating to ~3000 K at 135 GPa, Fp becomes ~5 times opaquer than it is at room temperature. In contrast, Bgm is only 20-30 % opaquer at ~3500 K than at room temperature. Because these transformations are fully reversible, they must reflect temperature-induced changes in light absorption by these single crystals. Our new streak camera data unambiguously show that light absorption in Fp is much more sensitive to temperature than in Bgm, confirming that the optical opacity of the lowermost mantle, and by extension its radiative conductivity, is governed by Fp. Such a diverse high-temperature behavior of Fp and Bgm likely results from the different mechanisms that govern light extinction in these phases. Even at room temperature single crystalline Fp with 13 mol.% Fe at 117 GPa is 2-3 times opaquer than Bgm with 6 mol.% Fe due to the intense Fe-O charge transfer band that extends into the VIS range. Lattice vibrations in hot Fp dynamically decrease the Fe-O separation, redshifting the Fe-O charge transfer band, narrowing the band gap, and serving as a physical

mechanism that effectively blocks radiative heat transport in the lowermost mantle. The proposed mechanism is much less effective in Bgm which accommodates iron predominantly at the larger (dodecahedral) site with longer average Fe-O distances than in Fp.

The high-pressure high-temperature behavior of Fp is of key importance for a pyrolytic model, indicating that Fp plays a major role in the opacity of the lower mantle and the effectiveness of radiative heat transport. In addition, the decreased band gap enhances electrical conductivity of Fp in the narrow depth range of the TBL (< 100 km) where the temperature increase is sharpest. Our interpretation of the optical behavior of Fp at high P-T is in qualitative agreement with the computational evidence for a very high electrical conductivity ( $\sim 4*10^4 \text{ S/m}$ ) in Fp at CMB conditions due to iron d-states forming broad bands near the Fermi level (Holmstrom and Stixrude, 2015). As such, our work hints that the physical properties of Fp contribute complexity to the CMB region and are responsible for some of its exotic features. For example, temperature-enhanced electrical conductivity of Fp in the TBL can account for the apparent absence of lag between the fluctuation in day length and geomagnetic jerks, which requires a thin (< 50 km) layer of highly conducting mantle just above the core (Holme and de Viron, 2013).

Firmly constrained total thermal conductivity at the base of the mantle offers valuable insights into the CMB heat flow through the Fourier law of heat conduction:  $Q_{CMB} = A_{CMB} * k_{total} * \Delta T$ , where  $A_{CMB}$  is the surface area of the CMB and  $\Delta T$  is the temperature gradient above the CMB. Experimental estimates of the lattice thermal conductivity for a 4:1 mixture of Bgm (or Ppv) and Fp at CMB conditions fall in the range of 7.7-8.8 W/m/K (Supplementary Table S3) (Dalton et al., 2013; Ohta et al., 2017; Okuda et al., 2017). While these values are based on measurements in DACs at 300 K and rely on extrapolations to CMB temperatures, they are consistent with *ab initio* calculations of lower mantle thermal conductivity (Stackhouse et al., 2015) as well as a recent experimental study of the lattice conductivity in Fe- and Fe,Al-bearing Bgm (Hsieh et al., 2017). Recent estimates of the total thermal conductivity at the base of the

mantle accepted  $k_{rad}$  of ~2-4 W/m/K (*e.g.* Ohta et al. (2017); Okuda et al. (2017)). The results of this work clearly indicate that radiative conductivity is not an important mechanism of heat transport in the lowermost mantle and may be safely neglected from estimates of the total thermal conductivity at the CMB. Accepting  $k_{total} \approx k_{lat} \approx 8.5$  W/m/K and a temperature gradient of ~0.007 K/m in the TBL (Stacey and Davis, 2008), we obtain a  $Q_{CMB}$  of ~ 8.5 TW for the present-day CMB.

This rate of heat extraction out of the core is sufficient to drive the present-day geodynamo, thanks to the compositional buoyancy due to the inner core growth, and is consistent with the inner core young age of  $\sim 0.6$ -1.3 Gy (e.g. Labrosse et al. (2001)), assuming radioactive heat production is small in the core. A much older Earth's magnetic record (Hadean-Paleoarchean) requires a geodynamo prior to the inner core nucleation, operating in a convecting liquid core. Two distinct scenarios follow from the low mantle thermal conductivity. If core thermal conductivity is relatively low (< 50 W/m/K) (Konopkova et al., 2016; Stacey and Loper, 2007), a CMB heat flux that is greater than the core adiabatic heat flux enables a thermallydriven geodynamo in the ancient fully molten core (Nimmo, 2015). Alternatively, high core thermal conductivity (> 100 W/m/K) (Ohta et al., 2016; Pozzo et al., 2012) is inconsistent with a thermally-driven geodynamo, and requires a compositionally-driven convection powered by light element exsolution upon core cooling (Badro et al., 2016; Hirose et al., 2017; O'Rourke and Stevenson, 2016). Even if an early geodynamo can be driven in the cooling ancient molten core, determining its exact driving mechanism requires a definitive assessment of Earth's core thermal conductivity. Beyond Earth's magnetic field, our results shed light on the plausibility of longlived dynamos in other terrestrial planets and exoplanets, and could provide a discriminating argument for their past or present habitability.

235

236

237

238

239

240

241

242

243

244

245

246

247

248

249

250

251

252

253

254

255

256

# Acknowledgements

260

261	SSL acknowledges the support of the Helmholtz Young Investigators Group CLEAR
262	(VH-NG-1325). This work was supported by the NSF Major Research Instrumentation program
263	DMR-1039807, NSF EAR-1520648 and NSF EAR/IF-1128867, the Army Research Office
264	(56122-CH-H), the National Natural Science Foundation of China (grant number 21473211), the
265	Chinese Academy of Sciences (grant number YZ201524), the Carnegie Institution of
266	Washington and Deep Carbon Observatory. The authors acknowledge T. Okuchi and N.
267	Purevjav for their assist with the synthesis of the brigdmanite sample at Okayama University at
268	Misasa. Parts of this work were conducted at GSECARS 13IDD beamline of the Advanced
269	Photon Source, Argonne National Laboratory. GeoSoilEnviroCARS (Sector 13), Advanced
270	Photon Source (APS), Argonne National Laboratory is supported by the National Science
271	Foundation – Earth Sciences (EAR-1128799) and Department of Energy – GeoSciences (DE-
272	FG02-94ER14466). This research used resources of the Advanced Photon Source, a U.S.
273	Department of Energy (DOE) Office of Science User Facility operated for the DOE Office of
274	Science by Argonne National Laboratory under Contract No. DE-AC02-06CH11357.

# References

275

278

279

280

281

282

283

284

285

Ammann, M.W., Brodholt, J.P., Wookey, J., Dobson, D.P., 2010. First-principles constraints on diffusion in lower-mantle minerals and a weak D " layer. Nature 465, 462-465.

Badro, J., Siebert, J., Nimmo, F., 2016. An early geodynamo driven by exsolution of mantle components from Earth's core. Nature 536, 326-328.

Clark, S.P., 1957. Radiative transfer in the Earth's mantle. Eos (formerly Trans. Am. Geophys. Union) 38, 931-938.

Dalton, D.A., Hsieh, W.P., Hohensee, G.T., Cahill, D.G., Goncharov, A.F., 2013. Effect of mass disorder on the lattice thermal conductivity of MgO periclase under pressure. Sci. Rep. 3, 02400.

Goncharov, A.F., Beck, P., Struzhkin, V.V., Haugen, B.D., Jacobsen, S.D., 2009. Thermal conductivity of lower-mantle minerals. Phys Earth Planet In 174, 24-32.

286 Goncharov, A.F., Haugen, B.D., Struzhkin, V.V., Beck, P., Jacobsen, S.D., 2008. Radiative 287 conductivity in the Earth's lower mantle. Nature 456, 231-234. 288 Goncharov, A.F., Lobanov, S.S., Tan, X., Hohensee, G.T., Cahill, D.G., Lin, J.F., Thomas, S.M., 289 Okuchi, T., Tomioka, N., 2015. Experimental study of thermal conductivity at high pressures: Implications 290 for the deep Earth's interior. Phys Earth Planet In 247, 11-16. 291 Goncharov, A.F., Struzhkin, V.V., Jacobsen, S.D., 2006. Reduced radiative conductivity of low-292 spin (Mg,Fe)O in the lower mantle. Science 312, 1205-1208. 293 Hirose, K., Morard, G., Sinmyo, R., Umemoto, K., Hernlund, J., Helffrich, G., Labrosse, S., 2017. 294 Crystallization of silicon dioxide and compositional evolution of the Earth's core. Nature 543, 99-102. 295 Hofmeister, A.M., 2014. Thermodynamic and optical thickness corrections to diffusive radiative 296 transfer formulations with application to planetary interiors. Geophys. Res. Lett. 41, 3074-3080. 297 Holme, R., de Viron, O., 2013. Characterization and implications of intradecadal variations in 298 length of day. Nature 499, 202-204. 299 Holmstrom, E., Stixrude, L., 2015. Spin crossover in ferropericlase from first-principles molecular 300 dynamics. Phys Rev Lett 114, 117202. 301 Hsieh, W.P., Deschamps, F., Okuchi, T., Lin, J.F., 2017. Reduced lattice thermal conductivity of 302 Fe-bearing bridgmanite in Earth's deep mantle. J. Geophys. Res. 122, 4900-4917. 303 Hulst, H.C.v.d., 1957. Light scattering by small particles. Wiley, New York,. 304 Irifune, T., Shinmei, T., McCammon, C.A., Miyajima, N., Rubie, D.C., Frost, D.J., 2010. Iron 305 Partitioning and Density Changes of Pyrolite in Earth's Lower Mantle. Science 327, 193-195. 306 Keppler, H., Dubrovinsky, L.S., Narygina, O., Kantor, I., 2008. Optical absorption and radiative 307 thermal conductivity of silicate perovskite to 125 Gigapascals. Science 322, 1529-1532. 308 Keppler, H., Kantor, I., Dubrovinsky, L.S., 2007. Optical absorption spectra of ferropericlase to 84 309 GPa. Am. Mineral. 92, 433-436. 310 Konopkova, Z., McWilliams, R.S., Gomez-Perez, N., Goncharov, A.F., 2016. Direct measurement

of thermal conductivity in solid iron at planetary core conditions. Nature 534, 99-101.

312 Labrosse, S., Poirier, J.P., Le Mouel, J.L., 2001. The age of the inner core. Earth Planet. Sci. Lett. 313 190, 111-123. 314 Lobanov, S.S., Holtgrewe, N., Lin, J.F., Goncharov, A.F., 2017. Radiative conductivity and 315 abundance of post-perovskite in the lowermost mantle. Earth Planet. Sci. Lett. 479, 43-49. 316 Nimmo, F., 2015. 8.02 - Energetics of the Core A2 - Schubert, Gerald, in: Schubert, G. (Ed.), 317 Treatise on Geophysics (Second Edition). Elsevier, Oxford, pp. 27-55. 318 O'Rourke, J.G., Stevenson, D.J., 2016. Powering Earth's dynamo with magnesium precipitation 319 from the core. Nature 529, 387-389. 320 Ohta, K., Kuwayama, Y., Hirose, K., Shimizu, K., Ohishi, Y., 2016. Experimental determination of the electrical resistivity of iron at Earth's core conditions. Nature 534, 95-98. 321 322 Ohta, K., Yagi, T., Hirose, K., Ohishi, Y., 2017. Thermal conductivity of ferropericlase in the Earth's 323 lower mantle. Earth Planet. Sci. Lett. 465, 29-37. 324 Okuda, Y., Ohta, K., Yagi, T., Sinmyo, R., Wakamatsu, T., Hirose, K., Ohishi, Y., 2017. The effect of 325 iron and aluminum incorporation on lattice thermal conductivity of bridgmanite at the Earth's lower 326 mantle. Earth Planet. Sci. Lett. 474, 25-31. 327 Pozzo, M., Davies, C., Gubbins, D., Alfe, D., 2012. Thermal and electrical conductivity of iron at 328 Earth's core conditions. Nature 485, 355-358. 329 Stacey, F.D., Davis, P.M., 2008. Physics of the Earth, 4th ed. Cambridge University Press, 330 Cambridge; New York. 331 Stacey, F.D., Loper, D.E., 2007. A revised estimate of the conductivity of iron alloy at high 332 pressure and implications for the core energy balance. Phys Earth Planet In 161, 13-18. 333 Stackhouse, S., Stixrude, L., Karki, B.B., 2015. First-principles calculations of the lattice thermal 334 conductivity of the lower mantle. Earth Planet. Sci. Lett. 427, 11-17. Thomas, S.M., Bina, C.R., Jacobsen, S.D., Goncharov, A.F., 2012. Radiative heat transfer in a 335 336 hydrous mantle transition zone. Earth Planet. Sci. Lett. 357, 130-136. 337 Ullrich, K., Langer, K., Becker, K.D., 2002. Temperature dependence of the polarized electronic

absorption spectra of olivines. Part I - fayalite. Phys Chem Miner 29, 409-419.

Supplementary material for online publication only Click here to download Supplementary material for online publication only: Pyrolite krad SL SUPPL.docx

\*Declaration of Interest Statement

The authors declare no conflict of interest